# Complete active space analysis of a reaction pathway: Investigation of the oxygen–oxygen bond formation

Han, Ruocheng ; Luber, Sandra

Abstract: Water nucleophilic attack is an important step in water oxidation reactions, which have been widely studied using density functional theory (DFT). Nevertheless, a single-determinant DFT picture may be insufficient for a deeper insight into the process, in particular during the oxygen–oxygen bond formation. In this work, we use complete active space self-consistent field calculations and describe an approach for a complete active space analysis along a reaction pathway. This is applied to the water nucleophilic attack at a Ru-based catalyst, which has successfully been used for efficient water oxidation and in silico design of new water oxidation catalysts recently.

DOI: https://doi.org/10.1002/jcc.26201

# Complete active space analysis of a reaction pathway: investigation of the oxygen-oxygen bond formation

R. Han[1] and S. Luber[1]

[1]*Institut für Chemie, Universität Zürich, Zürich, Switzerland*

**Abstract**

Water nucleophilic attack is an important step in water oxidation reactions, which have been widely studied using density functional theory (DFT). Nevertheless, a single-determinant DFT picture may be insufficient for a deeper insight into the process, in particular during the oxygen-oxygen bond formation. In this work, we use complete active space self-consistent field calculations and describe an approach for a complete active space analysis along a reaction pathway. This is applied to the water nucleophilic attack at a *Ru*-based catalyst, which has successfully been used for efficient water oxidation and in silico design of new water oxidation catalysts recently.

Keywords: multiconfigurational method, complete active space, reaction pathway, water oxidation, water nucleophilic attack. ■

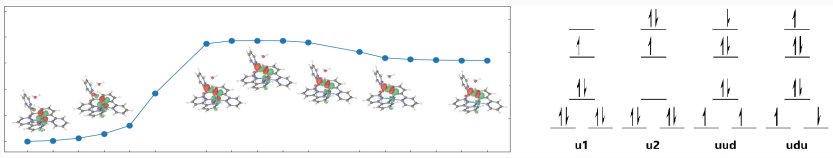


The water nucleophilic attack at a Ru-based water oxidation catalyst is investigated in detail based on an approach for complete active space calculations along the entire reaction pathway.

# Introduction

Water splitting, which encompasses water oxidation and reduction, has been investigated intensively over the past few decades as a potential solution for sustainable energy storage and conversion. Various molecular structures, e.g. manganese clusters[1–3], cobalt cubanes[4–11], and ruthenium polypyridyl complexes[12–17] (see e.g. reviews in Refs.[11,18–22]), have been proposed as potential water oxidation catalysts. Mechanistic studies are of special interest since they provide a better understanding of catalytic cycles and can further offer guidance on the modification of reactions. While computational studies about the above-mentioned systems (see e.g. Refs.[23–38]) on structural stability and reaction pathways have been published, mostly only a general picture of reaction related species, e.g. reactants, transition states, intermediates, and products, based on energy criteria has been reported using Kohn–Sham DFT[39]. While DFT calculations often provide accurate nuclear structures, they can produce an incorrect description of the electronic structure, leading to difficulties in e.g. dealing with near-degeneracy in bond breaking/formation processes[40,41] or low-energy spin states of transition metal complexes[42–44], which can be of significance when one would like to have a deeper view into chemical reactions.

Multiconfigurational wavefunction-based methods allow multiple determinants to describe the electronic structure. Depending on the system of interest, certain molecular orbitals may be highly correlated, so that their occupation numbers deviate from integer values. The combinatorial growth of computational cost with respect to the number of electrons and molecular orbitals prevents the fully multiconfigurational treatment of large systems. Based on this, complete active space self-consistent field[45,46] (CASSCF) has been invented, in which an active space is defined and only molecular orbitals in it are explicitly correlated. Only a few works using multiconfigurational methods have been published in the field of water oxidation. Kurashige *et al.*[47] focused on the formation of the *O*-*O* bond in $[H_4Fe_2O_7]^{2+}$ and investigated it with different methods including DFT, CASSCF, CASPT2 (complete active space second-order perturbation) and MRCI (multireference configuration interaction). Fernando and Aikens[48] presented a water oxidation cycle of a *Mn* dimer catalyst and analyzed structures of the different states of the catalytic cycle in detail with various wavefunction-based methods.

The selection of the active space is usually empirical, and CASSCF calculations have thus

been challenging and mainly based on chemical intuition. Also, the molecular orbitals selected are not guaranteed to remain in the active space during the CASSCF calculation, leading to a type of inconsistency problem (Type I). Moreover, CASSCF calculations for different nuclear structures of the same molecule (e.g. analysis of structures in a reaction pathway) easily encounter the issue that the active space is not comparable among different nuclear structures, which is another type of inconsistency problem (Type II). Type I inconsistencies can be a guidance for the determination of the active space, because highly correlated orbitals tend to switch into while non-correlated ones switch out of the active space during the CASSCF calculation. Type II inconsistencies happen when the types of correlated orbitals vary due to change of the nuclear geometry. They can affect the analysis of the reaction pathway, since comparability is hampered and correlation information is lost when orbitals switch out of the active space and one is unsure if it is an artificial effect. Various approaches have been suggested for choosing active spaces[49–64]. In contrast to that, only a few approaches for a consistent complete active space analysis of reaction pathways for non-trivial systems have been published. The atomic valence active space (AVAS) method[65] has been introduced to generate the initial guess for CASSCF calculations by maximizing the given atomic valence character, and its application to one example, namely the Fenton reaction, was demonstrated, however using complete active space configuration interaction instead of CASSCF. Another approach has been based on the orbital entanglement method[66,67], which has been used for the consistent selection of orbital active spaces along reaction coordinates and applied to isomerization[53] and Diels-Alder reactions[68,69]. The entanglement measure, however, may not be provided in commonly used programs and up to 4-electron reduced density matrix elements are required to derived the two-orbital reduced density matrix.

In the following, we employ a simple systematic process for construction of a reaction pathway, by which one can analyze the reaction at a multiconfigurational level for certain nuclear structures given for the reaction path. The focus of the described approach is not on the generation of nuclear structures, for which various methods such as nudged elastic band (NEB)[70–73] or intrinsic reaction coordinate (IRC)[74] can be used, but on the choice and analysis of the active space for the CAS calculations. The scheme of active space selection aims at the consistency of orbitals along the reaction pathway, thus providing a detailed picture of the electronic structure evolution. A Ru-based catalyst, *trans*-[$Ru^{V}$(O)(Cl)(L-OMe-$\kappa$-$N^4$)]$^{2+}$ (L-OMe: 6,6”-

(methoxy(pyridin-2-yl)methylene)di-2,2'-bipyridine) (Ru(O)(Cl)Py5OMe), is used as a model system to investigate the water nucleophilic attack (WNA) in the water oxidation process. This catalyst has been found experimentally to be an efficient water oxidation catalyst[13] and has been used for in silico catalyst design recently in our group as well[28]. The catalyst offers the advantage that its nuclear structure is clearly defined. In particular the octahedral coordination of the nuclear structure is rather rigid compared to other coordination types. Moreover, a pyridine ring in the structure can act as an intramolecular base in the WNA process. A radical coupling mechanism, which has also commonly been found in water oxidation catalysis, can be excluded due to the first-order reaction kinetics measured in experiment[13]. The first work[13] of this system has revealed structural information of the associated reactant (AR), the transition state (TS) structure, and the associated product (AP) involved in the WNA process from DFT calculations. Subsequent work[28] has targeted variations of the functional groups of the (Ru(O)(Cl)Py5OMe) system and DFT calculations have been carried out to provide general design concepts for such type of catalysts. This work focuses on an in-depth investigation of the electronic structure along the WNA reaction pathway of the original system[13] going beyond the standard DFT approach by using calculations on the multiconfigurational level.

# Methods

## Consistent active space selection

Three geometries, namely, the AR, TS, and AP, for the WNA at the Ru(O)(Cl)Py5OMe catalyst during water oxidation catalysis optimized with DFT in the doublet spin state are taken from previous work[13] (see Fig. 1).

Spin multiplicity is 2 (doublet spin state) for all calculations in this work. Wavefunction-based calculations were carried out using the *OpenMolcas* program[75,76] with the valence triple-zeta polarization (ANO-RCC-VTZP) basis set for the ruthenium (*Ru*) atom and valence double-zeta polarization (ANO-RCC-VDZP) basis set for the other atoms[77,78]. Localization of either occupied orbitals or unoccupied orbitals obtained from a restricted open-shell Hartree–Fock (ROHF) calculation was performed using the Pipek–Mezey procedure[79]. Analogous calculations using unrestricted HF as input for the localization gave similar results. Localized molec-

ular orbitals (LMOs) were atomic-orbital (AO)-type like, which alleviated the choice of LMOs for the active space. Then the CASSCF calculation with the initial guess of selected active orbitals was performed. After that, consistency of the natural orbitals (NOs) before and after the CASSCF calculation was checked to detect Type I problems, i.e. cases where a selected orbital switch out of the active space. In detail, if NOs switched out of the active space, then they were removed from the initial guess; while those which switched into the active space during the CASSCF calculation were added to the initial guess for further CASSCF calculations. As standardly done for such calculations, this was carried out during the CASSCF calculation until no orbital switched in or out of the active space. This was carried out for the AR, TS, and AP geometries with the same computational settings and initial guess for the active space (the procedure is also sketched in Fig. 2). At last, consistency of the active space among the three geometries was checked for Type II problems, for which the second loop is needed as shown in Fig. 2. The consistency checks of both loops were performed by checking the coefficients of the AO components inside the active space (vide infra for more details). A general challenge is that the active space can become too large to be treated with currently available methods. This, however, has been a common problem in this field. In our procedure, only the AR, TS, and AP frames were needed for the construction of the active space rather than all frames along the reaction pathway. This is valid if these three frames can represent the reaction in a sophisticated manner. Of course, more nuclear structures of the reaction pathway can be included in this analysis, in particular for more complex reaction processes.

## Reaction pathway construction

Frames along the reaction pathway from the AR to the TS and from the TS to the AP were generated and optimized by the woelfling chain-of-states method[80,81] using BP86[82,83]-D3[84]/def2-TZVP[85] as implemented in *Turbomole*[86,87] (version 7.3). It was found that electronic energies of optimized frames changed abruptly near the TS. Therefore, additional structures elongated along the imaginary normal mode of the TS involving the peroxide ($O_C$-$O_W$) bond were generated, since this normal mode reflects the change of the geometry from the reactant to the product. Then the frames generated by the latter and the woelfling method were compared and selected based on continuity of electronic energies, $O_C$-$O_W$ bond distances, and $O_W$-$H$ bond

distances (see Fig. 3). The selected frames together with the AR, TS, and AP geometries were taken for the reaction pathway.

## Complete active space calculations and analysis along the reaction pathway

Two methods were tested for CASSCF calculations along the reaction pathway: 1. All frames use the same initial guess of active orbitals as that of the TS (TSinitial, similar idea as described in Fig. 2); 2. From the TS to the AR and from the TS to the AP, the calculation of a frame always takes the result of the previous frame as the initial guess (Framewise), which is a variant not described in the Fig. 2 scheme. The transition state contains important information of the reaction studied and its nuclear structure is between the ones of the AR and the AP, which supports our choice of both approaches.

Consistency checks were carried out to confirm that the active space chosen is representative along the reaction pathway. Singular value decomposition (SVD) was performed on the NO overlap matrix of the active space before and after the CASSCF calculations since a singular value deviating from 1.0 can indicate an orbital which switched into/out of the active space (see Ref.[65]). The NO overlap matrix ($\boldsymbol{S}_{NOact}$, contains only the NO coefficients of the active orbitals) was computed as below (Eq. 1) by the AO overlap matrix ($\boldsymbol{S}_{AO}$) and the NO coefficient matrices before ($\boldsymbol{C}^{ini}$) and after ($\boldsymbol{C}^{fin}$) the CASSCF calculation. Similarly, Eq. 2 is used to calculate the NO overlap matrix between two different geometries (similar to Ref.[88] in the context of embedding) after the CASSCF calculations with $\boldsymbol{i}$ and $\boldsymbol{j}$ denoting two nuclear structures. Löwdin orthogonalization is adopted for the calculation of $\boldsymbol{S}_{AO}^{\frac{1}{2}}$. Also, the AO contributions ($\boldsymbol{R}_{AO}$, see Eq. 3) in the active space were calculated for each frame along the pathway where a small value implies low contribution of an AO in the frame. The analysis based on AOs ignored the contribution from the off-diagonal parts which we found to be negligible for the structures studied.

$$\boldsymbol{S}_{NOact} = (\boldsymbol{C}^{fin})^{\dagger} \boldsymbol{S}_{AO} (\boldsymbol{C}^{ini}) \tag{1}$$

$$\boldsymbol{S}^{ij}_{NOact} = (\boldsymbol{C}^j)^\dagger (\boldsymbol{S}^j_{AO})^{\frac{1}{2}} (\boldsymbol{S}^i_{AO})^{\frac{1}{2}} (\boldsymbol{C}^i) \tag{2}$$

$$\boldsymbol{R}_{AO} = diag((\boldsymbol{C}^{fin})(\boldsymbol{C}^{fin})^\dagger) \tag{3}$$

Besides the analysis of NO overlap matrices before and after a CASSCF calculation for one nuclear structure, different from previous works[65,69], the consistency check was additionally carried out by using NO overlaps between different nuclear structures and AO contributions of all frames along the reaction pathway.

# Results and Discussion

## Active space of the AR, TS, and AP structures

For the initial guess of the active orbitals for the TS, we selected various LMOs. Four of the $4d$ LMOs of the metal center ruthenium ($Ru$) were chosen whereas $Ru$ $4s$ and $4p$ LMOs were not included in the first place since we aimed at a construction of a relatively small active space. Also, $Ru$ $4d_{x^2-y^2}$ was left out considering that it matches the symmetry of orbitals of coordinated nitrogen ($N_C$) atoms and would presumably bring more orbitals ($2p$ orbitals of the pyridine rings) into the active space during the CASSCF calculation. In a similar manner, all valence orbitals of coordinated chlorine ($Cl$ $3s$ and $3p$ orbitals), coordinated oxygen ($O_C$ $2s$ and $2p$ orbitals) and water oxygen ($O_W$ $2s$ and $2p$ orbitals) were included in the active space. 16 orbitals were selected in the initial guess of the active space.

As shown in Table 1, the active space did not change anymore after two CASSCF calculations, which means that a consistent active space for the TS structure was found with an active space of 33 electrons and 19 orbitals (CAS(33,19)). The same process was carried out for the AR and AP structures with the same initial guess for the active space as used for the TS structure. Fortunately, we did not experience a severe Type II problem at the stage of construction of the active space, namely, converged active spaces were well comparable among the three geometries and we could skip the second loop described in Fig. 2. In a more general case, expansion of the active space can be needed if the Type II problem is not negligible.

Until now, a consistent active space for the AR, TS and AP structures was built. In order to have a more detailed reaction pathway, more nuclear structures were generated as described in the next section.

## Reaction pathway of the WNA

As mentioned in Section Methods, a combination of the woelfling approach and structures elongated along the imaginary normal mode of the TS was used to construct a pathway. Other approaches such as NEB and IRC can of course also be used. The selection of structures was based on three factors: electronic energy, $O_C$-$O_W$ distance and $O_W$-$H$ distance (see Fig. 3). We aimed at a smooth energy profile (see Fig. 4 for the abrupt change in the energy profile using the woelfling approach only) and monotonous changes of $O_C$-$O_W$ and $O_W$-$H$ bonds along the pathway. Taking these aspects into consideration, frames 1 to 5 and frames 7 to 11 generated by the woelfling approach as well as elongated structures (labelled NM-2, NM-1, NM1, and NM2 in the following) were chosen. The result is shown in Fig. 5.

## Analysis of the CASSCF calculations

### TSinitial and Framewise schemes

Results of the TSinitial (the initial guess of the frame TS as the initial guess) and the Framewise (the result of the previous frame as the initial guess) schemes are compared in terms of the electronic energy from the CASSCF calculations in Table 2. The electronic energy values of the two schemes are very close with less than 0.05 kcal/mol differences. The electronic energies obtained with the Framewise scheme are always equal to or lower than those obtained with the TSinitial scheme. Therefore, the following analysis is based on the results employing the Framewise scheme.

SVD of NO overlap matrices constructed from the same nuclear structure (see Eq. 1) showed that Frame 4, NM-2 and NM2 have relative low values ($<$0.6), indicating orbital switching. Similar results were obtained from SVD between the corresponding nuclear structures (see Eq. 2). To investigate this in detail, the calculation of AO contributions was carried out.

From the normalized AO contributions (Fig. 10), it is obvious that most of the orbitals

remain 90 % inside the active space along the reaction pathway. However, the $2s$ $2p_x$ $2p_y$ $2p_z$ contributions at the $O_W$ atom have low contributions near the AR structure and the $3p_y$ AO of $Cl$ has a low contribution near the AP, which means that NOs switched out of the active space. The $O_W$ orbitals which are partially outside the active space belong to the reactant water molecule, so the corresponding NOs have low electronic energies and are fully occupied in frames near the AR structure. This situation can hardly be avoided by excluding $O_W$ orbitals for the entire reaction pathway, because $O_W$ is one of the essential atoms involved in the reaction, the orbitals of which must be considered. Similarly, the NO with $Cl$ $3p_y$ contributions has relative low electronic energy near the AP structure, which explains the low contribution (partially out of the active space). Such kind of orbital switching can often not be prevented, especially when the reaction happens between molecules, if a relatively small active space is aimed at. It is difficult to make any statement about the effect of such orbital switching on the electronic energy but the effect should be reasonable, in particular if the orbital which switched out is not included in the reaction or plays not an important role with respect to the correlation energy. Enlarging the active space may alleviate such a situation. The energetic information obtained with CASPT2 calculations using the CASSCF references is also presented in Fig. 6.

### Analysis of configuration state functions and natural orbital occupation numbers

Fig. 7 shows the weight of major configuration state functions (CSFs) along the pathway. Four CSFs were selected since they have more than 1 % contribution to the wavefunction of at least one frame. CSFs are described with the notations **2**, **u**, **d** and **0**, which represent a fully occupied orbital, an orbital with one up spin electron, an orbital with one down spin electron, and an unoccupied orbital, respectively. The major CSFs found can be described by **22222222222222u00** (*abbr.* **u1**), **22222222222220222u20** (*abbr.* **u2**), **2222222u2u2222222d0** (*abbr.* **uud**), and **2222222u2d2222222u0** (*abbr.* **udu**). From Fig. 7, we can see that the weight of **u1** decreases near the TS. This indicates that the reaction happens because chemical reactions usually include a "mixed" mode of bond breaking and forming, which corresponds to a correlated electronic structure. Five NOs were chosen by comparing the differences of the four major CSFs, and the shapes of them are illustrated in Fig. 8. Considering the dominant AOs in these NOs, we denote them as follows: $\pi_{x,Ru-O_C}$ formed by $Ru$ $4d_{xz}$ and $O_C$ $2p_x$, $\pi_{y,Ru-O_C}$ formed by $Ru$ $4d_{yz}$ and $O_C$ $2p_y$, $\sigma_{y,O_C-O_W}$ formed by $O_C$ $2p_y$ and $O_W$ $2p_y$, $\pi^*_{x,Ru-O_C}$ formed by

*Ru* $4d_{xz}$ and $O_C$ $2p_x$, and $\sigma^*_{y,O_C-O_W}$ (denoted as $\pi^*_{y,Ru-O_C}$ near the AR later on) formed by *Ru* $4d_{yz}$, $O_C$ $2p_y$, and $O_W$ $2p_y$. The concerned NOs mentioned above are also shown in the description of CSFs in Table 3. We note that we only investigated the system with a doublet spin state. The quartet spin state of the structures was found to be significantly higher in electronic energy so the effect of other spin states or spin crossover was not further examined.

From **u1** to **u2**, a pair of electrons moves from $\sigma_{y,O_C-O_W}$ to $\sigma^*_{y,O_C-O_W}$, which represents a transition from the $O_C$-$O_W$ bonding orbital to the antibonding orbital (see Fig. 11 and Fig. 12). This is exactly where the reaction happens. The variation of the **u1** and **u2** weights near the TS shows that the $\sigma^*_{y,O_C-O_W}$ is partially occupied when the reaction occurs.

Fig. 9 shows that the natural orbital occupation number (NOON) of $\sigma_{y,O_C-O_W}$ deviates from 2.00 and the NOON of $\sigma^*_{y,O_C-O_W}$ deviates from 0.00 near the TS, the tendency of which directly shows the correlation between $\sigma_{y,O_C-O_W}$ and $\sigma^*_{y,O_C-O_W}$. By contrast, the NOONs of $\pi_{x,Ru-O_C}$, $\pi_{y,Ru-O_C}$, and $\pi^*_{x,Ru-O_C}$ generally have a monotonous change along the reaction pathway, with occupied NOs approaching 2.00, half occupied ones approaching 1.00 and unoccupied ones approaching 0.00. These tendencies provide the extra information that the AP is less correlated than the AR within the correlation effects covered by CASSCF. Other orbitals not shown in Fig. 9 are either considered fully occupied or unoccupied with NOONs greater than 1.99 or less than 0.01, except for $\sigma_{z,Ru-O_C}$ and $\sigma^*_{z,Ru-O_C}$ (mainly formed by *Ru* $4d_{z^2}$ and $O_C$ $2p_z$) which have non-trivial NOONs but are not mentioned here since they are not interesting for the WNA reaction.

An orbital diagram is given in Fig. 11 in order to suggest a possible way of formation of molecular orbitals (NOs for the **u1** CSF). *Ru* has three valence electrons with two in the $4d_{xy}$ and one in the $4d_{xz}$ AO, while $O_C$ and $O_W$ have their valence orbitals fully occupied. Then the $\pi_{x,Ru-O_C}$ $\pi_{y,Ru-O_C}$ bonding orbitals and their antibonding orbitals of *Ru*=$O_C$ are formed by overlaps of *Ru* $4d_{xz}$ and $4d_{yz}$ AOs with the $O_C$ $2p_x$ and $2p_y$ AOs, respectively, which can be seen in Fig. 8 in geometries along the reaction pathway. Lastly, *Ru*=$O_C$ $\pi^*_y$ and $O_W$ $2p_y$ form a $\sigma$-type bond, which is the $O_C$-$O_W$ bond as seen for geometries from NM-2 to AP in Fig. 8. We note here that the $\pi_{x,Ru-O_C}$, $\pi_{y,Ru-O_C}$, $\sigma_{y,O_C-O_W}$, $\pi^*_{x,Ru-O_C}$, and $\sigma^*_{y,O_C-O_W}$ orbitals in the diagram in Fig. 11 generally correspond to those shown in Fig. 8. Therefore, the four CSFs can also be sketched by these NOs (see Fig. 12).

By comparing **u1** with the other CSFs (see Fig. 12) one may regard the effect of the latter as

bond weakening effects, since **u2**, **uud**, and **udu** represent electronic transitions from bonding to antibonding orbitals (compare Fig. 11). CSF **u2** demonstrates a weakening effect of the bond between *Ru*=$O_C$ and $O_W$ by the transition of an electron pair from $\sigma_{y,O_C-O_W}$ to $\sigma^*_{y,O_C-O_W}$ without the formation of an unpaired electron, which we refer to as electron pair process in the following. CSFs **uud** and **udu** include a weakening effect of two bonds: the bond between *Ru*=$O_C$ and $O_W$ by a single occupation of $\sigma^*_{y,O_C-O_W}$; the bond between *Ru* and $O_C$ by the transition of a single electron from $\pi_{x,Ru-O_C}$ to $\pi^*_{x,Ru-O_C}$ and the loss of a single electron on the $\pi_{y,Ru-O_C}$. We call these processes single electron processes, since two extra single electrons are formed compared to **u1**. Weakening effects can be estimated from Fig. 12 and Table 4 by Eq. 4 with the weight $\boldsymbol{w_d}$ and the bond order $\boldsymbol{B.O.(d)}$ for CSF $\boldsymbol{d}$ where $\boldsymbol{d} = \boldsymbol{u1}, \boldsymbol{u2}, \boldsymbol{uud}, \boldsymbol{udu}$. Then it can be calculated that the contributions of the electron pair process and the single electron processes to the weakening effect of $O_C$-$O_W$ bond are roughly 92 % $\sim$ 96 % and 4 % $\sim$ 8 %, which indicates that the correlation effect during the reaction is mainly based on the electron pair process. Other NOs not shown here are either fully occupied or remain non-bonded along the reaction pathway.

$$weakening = \sum_{\boldsymbol{d}\in\{\boldsymbol{u1},\boldsymbol{u2},\boldsymbol{uud},\boldsymbol{udu}\}} \boldsymbol{w_d} \cdot (\boldsymbol{B.O.(u1)} - \boldsymbol{B.O.(d)}) \tag{4}$$

Fig. 13 shows possible mechanisms for the WNA that **u2**, **uud**, and **udu** may belong to. In the electron pair process, a pair of electrons from the water molecule transfers to $\pi^*_{y,Ru-O_C}$ (later on $\sigma^*_{y,O_C-O_W}$ in the pathway, see Fig. 8), which forms configuration **u2**. Then the $O_C$-$O_W$ bond is formed as the result of a $\sigma^*_{y,O_C-O_W}$ to $\sigma_{y,O_C-O_W}$ transition. The electron pair process corresponds to a classical WNA[11]. In the single electron process, a single electron (either with up or down spin) moves from water to $\pi^*_{y,Ru-O_C}$ (later on $\sigma^*_{y,O_C-O_W}$ in the pathway, see Fig. 8), and the $O_C$-$O_W$ bond is formed by the remaining single electron on water and one of the electrons in $\pi^*_{x,Ru-O_C}$ or $\pi^*_{y,Ru-O_C}$. The resulting configurations are **uud** and **udu**, and the single electron process resembles a single electron transfer-water nucleophilic attack[89].

# Conclusion

We have studied in detail the WNA at the *trans*-[$Ru^{V}$(O)(Cl)(L-OMe-$\kappa$-$N^4$)]$^{2+}$ water oxidation catalyst using a multiconfigurational approach. In order to investigate the reaction pathway beyond the standard DFT picture using only the AR, TS, and AP structures, a simple approach of active space selection along a reaction path is proposed in this work. The focus of this scheme has been on prevention of Type I and Type II inconsistencies, i.e. orbitals switching out of the active space during a CASSCF calculation and inconsistent active spaces between different nuclear structures. Consistency has been checked by SVD of overlap matrices for a single nuclear structure or between two nuclear structures and the normalized AO contributions along the reaction pathway. In more detail, for the WNA reaction studied, we first took the AR, TS, and AP structures optimized by DFT and used a designed-scheme of CASSCF calculations to construct a widely consistent active space, which was found to be an active space CAS(33,19) for these three structures. Then the reaction pathway with 14 additional frames was generated using DFT calculations featuring smooth changes in the electronic energy and the nuclear geometry. CAS(33,19) calculations of 17 structures in total were carried out using two variants for CASSCF calculations along the reaction pathway, namely the TSinitial and Framewise schemes, both of which gave the similar result that the designed active space is mostly consistent for all frames.

The analysis of weights of CSFs and NOONs provided a detailed insight into the varying electronic structure during the reaction. By this approach, non-negligible correlation was observed in the WNA of the investigated *Ru*-based catalyst, leading to fractional occupation numbers of the $\pi_{x,Ru-O_C}$, $\pi_{y,Ru-O_C}$, $\sigma_{y,O_C-O_W}$, $\pi^*_{x,Ru-O_C}$, and $\sigma^*_{y,O_C-O_W}$ NOs.

An orbital diagram is proposed to explain the correlation effect from a chemical point of view, with NOs reduced to AOs. Moreover, the correlation effect obtained from the CASSCF calculations is interpreted in a more intuitive way as weakening of chemical bonds by the transitions from bonding to antibonding orbitals. Bond orders or other chemically intuitive information can be extracted and calculated from the results. In the case of the WNA reaction of the water oxidation catalyst under investigation, four major electron configurations contribute to the reaction, and weakening of the $O_C$-$O_W$ bond is found near the TS. The bond weakening effect comes from non-dominant CSFs, indicating that both an electron pair process and single

electron processes exist on the formation of the $O_C$-$O_W$ bond. Moreover, in both processes, $\sigma^*_{y,O_C-O_W}$ composed of *Ru* $4d_{yz}$, $O_C$ $2p_y$, and $O_W$ $2p_y$ has been found to play a role. While the calculations presented here have aimed at a rather small consistent active space within the CASSCF approach, future calculations may focus on the influence of larger active spaces and dynamic correlation as well as different spin state(s) on the WNA reaction.

The results provide a compelling evidence that single determinant methods are not enough for the description of electron redistribution during the WNA reaction studied and multiconfiguration analysis is required to provide a guidance in the targeted development of such catalysts based on the in-depth analysis of orbitals. While it is difficult to directly tune orbitals for more efficient processes, some indirect ways like modifications of surroundings (dielectric constant, ligand field, etc.) may be adopted, also for improving the energetic alignment of molecular orbitals important for other catalytic steps.

In summary, we have studied in detail the oxygen-oxygen bond formation during the WNA at a Ru-based complex which has recently been shown to be an efficient and stable catalyst for water oxidation. For the complete active space analysis, we have used an approach, which aims at consistent active space selection along the reaction pathway, using a systematic process including derivation of the active space, construction of the reaction pathway and check of consistency. This has revealed the importance and behaviour of certain natural orbitals in this reaction, which provides essential insight highly sought-for for the analysis and design of such compounds.

## Acknowledgment

Funding by the University of Zurich, the Swiss National Science Foundation (grant no: PP00P2_170667), and the University Research Priority Program LightChEC is gratefully acknowledged. We thank Giovanni Li Manni and Mauro Schilling for general discussions and the Swiss National Supercomputing Center for computing resources (project ID: s745 and s788).

# References


1. C. Zhang, C. Chen, H. Dong, J.-R. Shen, H. Dau, J. Zhao, *Science* **2015**, *348*, 690–693.
2. S. Mukherjee, J. A. Stull, J. Yano, T. C. Stamatatos, K. Pringouri, T. A. Stich, K. A. Abboud, R. D. Britt, V. K. Yachandra, G. Christou, *Proc. Natl. Acad. Sci. U. S. A.* **2012**, *109*, 2257–2262.
3. J. S. Kanady, E. Y. Tsui, M. W. Day, T. Agapie, *Science* **2011**, *333*, 733–736.
4. F. Evangelisti, R. Güttinger, R. Moré, S. Luber, G. R. Patzke, *J. Am. Chem. Soc.* **2013**, *135*, 18734–18737.
5. F. Evangelisti, R. Moré, F. Hodel, S. Luber, G. R. Patzke, *J. Am. Chem. Soc.* **2015**, *137*, 11076–11084.
6. F. Song, R. Moré, M. Schilling, G. Smolentsev, N. Azzaroli, T. Fox, S. Luber, G. R. Patzke, *J. Am. Chem. Soc.* **2017**, *139*, 14198–14208.
7. N. S. McCool, D. M. Robinson, J. E. Sheats, G. C. Dismukes, *J. Am. Chem. Soc.* **2011**, *133*, 11446–11449.
8. G. La Ganga, F. Puntoriero, S. Campagna, I. Bazzan, S. Berardi, M. Bonchio, A. Sartorel, M. Natali, F. Scandola, *Faraday Discuss.* **2012**, *155*, 177–190.
9. A. I. Nguyen, M. S. Ziegler, P. Oña-Burgos, M. Sturzbecher-Hohne, W. Kim, D. E. Bellone, T. D. Tilley, *J. Am. Chem. Soc.* **2015**, *137*, 12865–12872.
10. P. F. Smith, L. Hunt, A. B. Laursen, V. Sagar, S. Kaushik, K. U. D. Calvinho, G. Marotta, E. Mosconi, F. De Angelis, G. C. Dismukes, *J. Am. Chem. Soc.* **2015**, *137*, 15460–15468.
11. M. Schilling, S. Luber, *Front. Chem.* **2018**, *6*, 100.
12. D. Scherrer, M. Schilling, S. Luber, T. Fox, B. Spingler, R. Alberto, C. J. Richmond, *Dalton Trans.* **2016**, *45*, 19361–19367.
13. M. Gil-Sepulcre, M. Böhler, M. Schilling, F. Bozoglian, C. Bachmann, D. Scherrer, T. Fox, B. Spingler, C. Gimbert-Suriñach, R. Alberto, R. Bofill, X. Sala, S. Luber, C. J. Richmond, A. Llobet, *ChemSusChem* **2017**, *10*, 4517–4525.

14. L. Tong, L. Duan, Y. Xu, T. Privalov, L. Sun, *Angw. Chem. Int. Ed.* **2011**, *50*, 445–449.

15. L. Duan, L. Wang, A. K. Inge, A. Fischer, X. Zou, L. Sun, *Inorg. Chem.* **2013**, *52*, 7844–7852.

16. L. Duan, F. Bozoglian, S. Mandal, B. Stewart, T. Privalov, A. Llobet, L. Sun, *Nat. Chem.* **2012**, *4*, 418–423.

17. H. Tseng, R. Zong, J. T. Muckerman, R. Thummel, *Inorg. Chem.* **2008**, *47*, 11763–11773.

18. D. W. Shaffer, Y. Xie, J. J. Concepcion, *Chem. Soc. Rev.* **2017**, *46*, 6170–6193.

19. M. D. Kärkäs, B. Åkermark, *Chem. Rev.* **2016**, *16*, 940–963.

20. Q. Zeng, F. W. Lewis, L. M. Harwood, F. Hartl, *Coord. Chem. Rev.* **2015**, *304*, 88–101.

21. M. D. Kärkäs, O. Verho, E. V. Johnston, B. Åkermark, *Chem. Rev.* **2014**, *114*, 11863–12001.

22. R. Cao, W. Lai, P. Du, *Energy Environ. Sci.* **2012**, *5*, 8134–8157.

23. F. H. Hodel, S. Luber, *ACS Catal.* **2016**, *6*, 1505–1517.

24. F. H. Hodel, S. Luber, *ACS Catal.* **2016**, *6*, 6750–6761.

25. M. Schilling, F. Hodel, S. Luber, *ChemSusChem* **2017**, *10*, 4561–4569.

26. A. Fernando, C. M. Aikens, *J. Phys. Chem. C* **2015**, *119*, 11072–11085.

27. L. Wang, T. Van Voorhis, *J. Phys. Chem. Lett.* **2011**, *2*, 2200–2204.

28. M. Schilling, M. Böhler, S. Luber, *Dalton Trans.* **2018**, *47*, 10480–10490.

29. Y. Liu, S. Ng, S. Yiu, W. W. Y. Lam, X. Wei, K. Lau, T. Lau, *Angw. Chem. Int. Ed.* **2014**, *53*, 14468–14471.

30. D. Moonshiram, Y. Pineda-Galvan, D. Erdman, M. Palenik, R. Zong, R. Thummel, Y. Pushkar, *J. Am. Chem. Soc.* **2016**, *138*, 15605–15616.

31. S. Zhan, D. Mårtensson, M. Purg, S. C. Kamerlin, M. S. Ahlquist, *Angw. Chem. Int. Ed.* **2017**, *56*, 6962–6965.

32. J. Nyhlén, L. Duan, B. Åkermark, L. Sun, T. Privalov, *Angw. Chem. Int. Ed.* **2010**, *49*, 1773–1777.

33. Y. Xie, D. W. Shaffer, J. J. Concepcion, *Inorg. Chem.* **2018**, *57*, 10533–10542.

34. S. Zhan, R. Zou, M. S. G. Ahlquist, *ACS Catal.* **2018**, *8*, 8642–8648.

35. Y. Wang, S. Zhan, M. S. G. Ahlquist, *Organometallics* **2018**, *38*, 1264–1268.

36. N. Govindarajan, A. Tiwari, B. Ensing, E. J. Meijer, *Inorg. Chem.* **2018**, *57*, 13063–13066.

37. R. Kang, K. Chen, J. Yao, S. Shaik, H. Chen, *Inorg. Chem.* **2014**, *53*, 7130–7136.

38. A. M. Asaduzzaman, D. Wasylenko, C. P. Berlinguette, G. Schreckenbach, *J. Phys. Chem. C* **2015**, *119*, 242–250.

39. W. Kohn, L. J. Sham, *Phys. Rev.* **1965**, *140*, A1133–A1138.

40. M. Radoń, K. Pierloot, *J. Phys. Chem. A* **2008**, *112*, 11824–11832.

41. J. Oláh, J. N. Harvey, *J. Phys. Chem. A* **2009**, *113*, 7338–7345.

42. A. Ghosh, T. Vangberg, E. Gonzalez, P. Taylor, *J. Porphyr. Phthalocyanines.* **2001**, *5*, 345–356.

43. A. Ghosh, B. J. Persson, P. R. Taylor, *J. Biol. Inorg. Chem.* **2003**, *8*, 507–511.

44. A. Ghosh, P. R. Taylor, *Curr. Opin. Chem. Biol.* **2003**, *7*, 113–124.

45. B. O. Roos, P. R. Taylor, P. E. Siegbahn, *Chem. Phys.* **1980**, *48*, 157–173.

46. P. E. Siegbahn, J. Almlöf, A. Heiberg, B. O. Roos, *J. Chem. Phys.* **1981**, *74*, 2384–2396.

47. Y. Kurashige, M. Saitow, J. Chalupskỳ, T. Yanai, *Phys. Chem. Chem. Phys.* **2014**, *16*, 11988–11999.

48. A. Fernando, C. M. Aikens, *Phys. Chem. Chem. Phys.* **2015**, *17*, 32443–32454.

49. J. M. Bofill, P. Pulay, *J. Chem. Phys.* **1989**, *90*, 3637–3646.

50. S. Keller, K. Boguslawski, T. Janowski, M. Reiher, P. Pulay, *J. Chem. Phys.* **2015**, *142*, 244104.

51. M. L. Abrams, C. D. Sherrill, *Chem. Phys. Lett.* **2004**, *395*, 227–232.

52. K. Boguslawski, P. Tecmer, G. Barcza, Ö. Legeza, M. Reiher, *J. Chem. Theory Comput.* **2013**, *9*, 2959–2973.

53. Y. Zhao, K. Boguslawski, P. Tecmer, C. Duperrouzel, G. Barcza, Ö. Legeza, P. W. Ayers, *Theor. Chem. Acc.* **2015**, *134*, 120.

54. M. Mottet, P. Tecmer, K. Boguslawski, Ö. Legeza, M. Reiher, *Phys. Chem. Chem. Phys.* **2014**, *16*, 8872–8880.

55. P. Pulay, T. P. Hamilton, *J. Chem. Phys.* **1988**, *88*, 4926–4933.

56. H. J. A. Jensen, P. Jørgensen, H. Ågren, J. Olsen, *J. Chem. Phys.* **1988**, *88*, 3834–3839.

57. S. Wouters, T. Bogaerts, P. V. D. Voort, V. V. Speybroeck, D. V. Neck, *J. Chem. Phys.* **2014**, *140*, 241103.

58. B. O. Roos, *Advances in Chemical Physics: Ab Initio Methods in Quantum Chemistry Part 2* **1987**, *69*, 399–445.

59. K. Pierloot, *Computational Organometallic Chemistry*, **2001**, pp. 123–185.

60. K. Pierloot, *Mol. Phys.* **2003**, *101*, 2083–2094.

61. V. Veryazov, P. Å. Malmqvist, B. O. Roos, *Int. J. Quant. Chem.* **2011**, *111*, 3329–3338.

62. A. Khedkar, M. Roemelt, *J. Chem. Theory Comput.* **2019**, *15*, 3522–3536.

63. E. R. Sayfutyarova, S. Hammes-Schiffer, *J. Chem. Theory Comput.* **2019**, *15*, 1679–1689.

64. J. J. Bao, S. S. Dong, L. Gagliardi, D. G. Truhlar, *J. Chem. Theory Comput.* **2018**, *14*, 2017–2025.

65. E. R. Sayfutyarova, Q. Sun, G. K. Chan, G. Knizia, *J. Chem. Theory Comput.* **2017**, *13*, 4063–4078.

66. Ö. Legeza, J. Sólyom, *Phys. Rev. B* **2003**, *68*, 195116.

67. J. Rissler, R. M. Noack, S. R. White, *Chem. Phys.* **2006**, *323*, 519–531.

68. C. J. Stein, M. Reiher, *J. Chem. Theory Comput.* **2016**, *12*, 1760–1771.

69. C. J. Stein, M. Reiher, *CHIMIA* **2017**, *71*, 170–176.

70. H. JÓNSSON, G. MILLS, K. W. JACOBSEN, *Classical and Quantum Dynamics in Condensed Phase Simulations*, **1998**.

71. G. Henkelman, H. Jónsson, *J. Chem. Phys.* **2000**, *113*, 9978–9985.

72. G. Henkelman, B. P. Uberuaga, H. Jónsson, *J. Chem. Phys.* **2000**, *113*, 9901–9904.

73. D. Sheppard, R. Terrell, G. Henkelman, *J. Chem. Phys.* **2008**, *128*, 134106.

74. K. Fukui, *Acc. Chem. Res.* **1981**, *14*, 363–368.

75. F. Aquilante, J. Autschbach, R. K. Carlson, L. F. Chibotaru, M. G. Delcey, L. D. Vico, I. F. Galván, N. Ferré, L. M. Frutos, L. Gagliardi, M. Garavelli, A. Giussani, C. E. Hoyer, G. L. Manni, H. Lischka, D. Ma, P. Å. Malmqvist, T. Müller, A. Nenov, M. Olivucci, T. B. Pedersen, D. Peng, F. Plasser, B. Pritchard, M. Reiher, I. Rivalta, I. Schapiro, J. Segarra-Martí, M. Stenrup, D. G. Truhlar, L. Ungur, A. Valentini, S. Vancoillie, V. Veryazov, V. P. Vysotskiy, O. Weingart, F. Zapata, R. Lindh, *J. Comput. Chem.* **2016**, *37*, 506–541.

76. P. Malmqvist, A. Rendell, B. O. Roos, *J. Phys. Chem.* **1990**, *94*, 5477–5482.

77. B. O. Roos, R. Lindh, P. Malmqvist, V. Veryazov, P. Widmark, *J. Phys. Chem. A* **2004**, *108*, 2851–2858.

78. B. O. Roos, R. Lindh, P. Malmqvist, V. Veryazov, P. Widmark, *J. Phys. Chem. A* **2005**, *109*, 6575–6579.

79. J. Pipek, P. G. Mezey, *J. Chem. Phys.* **1989**, *90*, 4916–4926.

80. P. Plessow, *J. Chem. Theory Comput.* **2013**, *9*, 1305–1310.

81. T. A. Halgren, W. N. Lipscomb, *Chem. Phys. Lett.* **1977**, *49*, 225–232.

82. A. D. Becke, *Phys. Rev. A* **1988**, *38*, 3098–3100.

83. J. P. Perdew, *Phys. Rev. B* **1986**, *33*, 8822–8824.

84. S. Grimme, *J. Comput. Chem.* **2006**, *27*, 1787–1799.

85. F. Weigend, R. Ahlrichs, *Phys. Chem. Chem. Phys.* **2005**, *7*, 3297–3305.

86. *TURBOMOLE V7.3 2018, a development of University of Karlsruhe and Forschungszentrum Karlsruhe GmbH, 1989-2007, TURBOMOLE GmbH, since 2007; available from* `http://www.turbomole.com`.

87. R. Ahlrichs, M. Bär, M. Häser, H. Horn, C. Kölmel, *Chem. Phys. Lett.* **1989**, *162*, 165–169.

88. M. Welborn, F. R. Manby, T. F. Miller, *J. Chem. Phys.* **2018**, *149*, 144101.

89. L. Bernasconi, A. Kazaryan, P. Belanzoni, E. J. Baerends, *ACS Catal.* **2017**, *7*, 4018–4025.

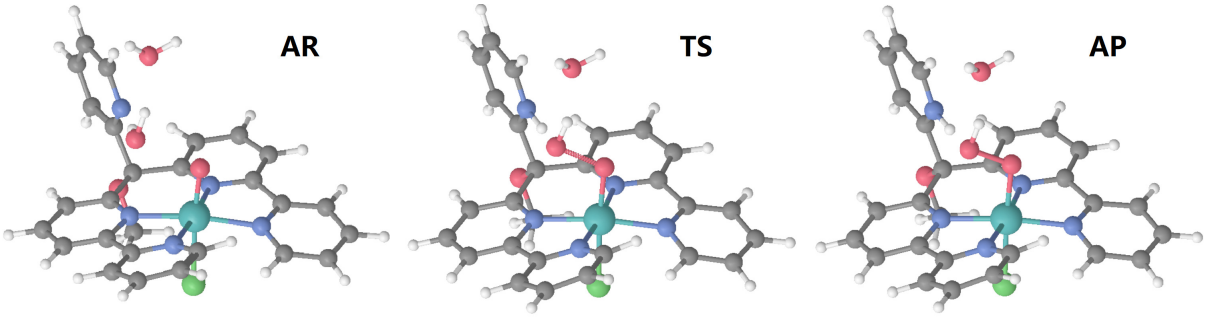


Figure 1: Optimized structures of AR, TS, and AP. Grey: carbon, white: hydrogen, red: oxygen, blue: nitrogen, green: chlorine, teal: ruthenium.

Consistent active space construction

**procedure** ACTIVESPACESELECTION(*geometries*)
    Initial calculations (e.g. ROHF) of *geometries*
    Localization of molecular orbitals of *geometries*
    Selection of localized orbitals from one of *geometries*: *ActiveSpace* ▷ geometry TS in our case
    $TypeII \leftarrow true$
    **while** *TypeII* is *true* **do**
        **for all** $A \in geometries$ **do**
            $ActiveSpace(A_{ini}) \leftarrow ActiveSpace$
            $TypeI \leftarrow true$
            **while** *TypeI* is *true* **do**
                CASSCF calculation of $A$ with $ActiveSpace(A_{ini})$: $ActiveSpace(A)$
                **if** $ActiveSpace(A_{ini})$ and $ActiveSpace(A)$ not consistent **then**
                    $ActiveSpace(A_{ini}) \leftarrow ActiveSpace(A)$
                **else**
                    $TypeI \leftarrow false$
                **end if**
            **end while**
        **end for**
        **if** $ActiveSpace(A)$ not consistent for $A \in geometries$ **then**
            $ActiveSpace \leftarrow \bigcup_{A \in geometries} ActiveSpace(A)$
        **else**
            $TypeII \leftarrow false$
        **end if**
    **end while**
    **return** *ActiveSpace*
**end procedure**

Figure 2: Procedure for the complete active space construction.

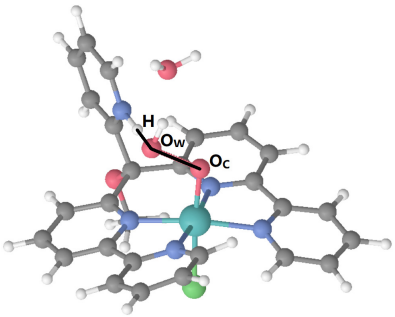


Figure 3: $O_C$-$O_W$ and $O_W$-$H$ bonds in *trans*-[$Ru^{V}$(O)(Cl)(L-OMe-$\kappa$-$N^{4}$)]$^{2+}$.

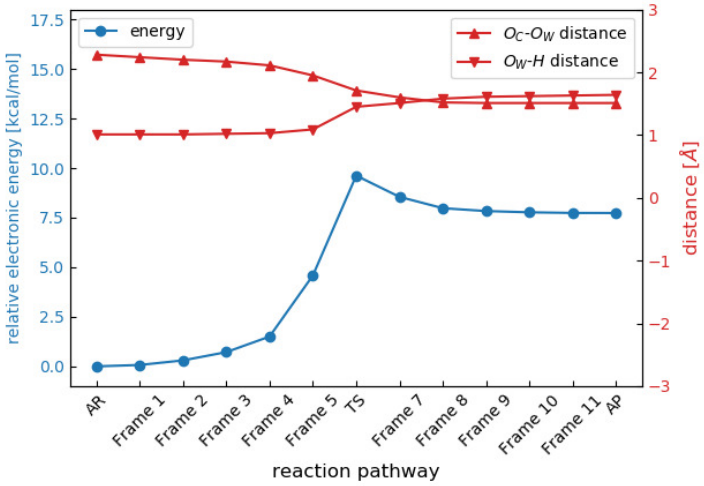


Figure 4: Relative electronic energy, $O_C$-$O_W$ distance and $O_W$-$H$ distance of frames generated by the woelfling approach.

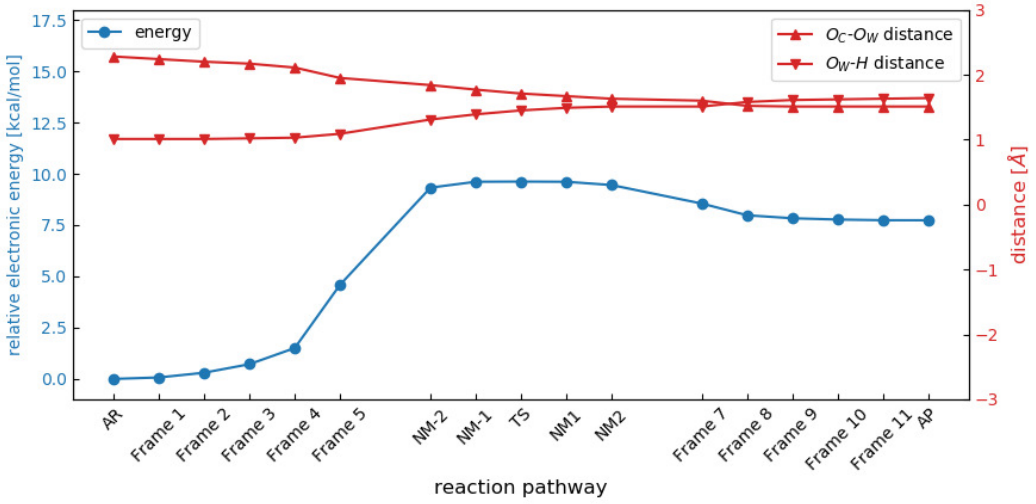


Figure 5: Relative electronic energy, $O_C$-$O_W$ distance and $O_W$-$H$ distance of the constructed reaction pathway using the woelfling and the imaginary normal mode calculations.

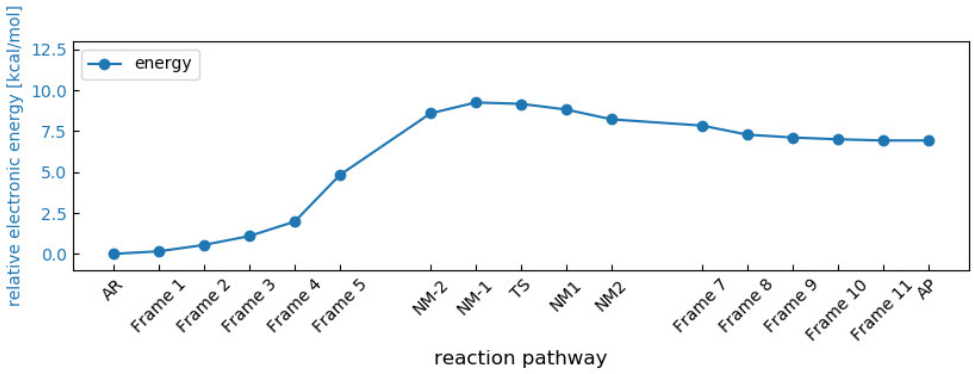


Figure 6: Relative electronic energy obtained from CASPT2 calculations along the reaction pathway.

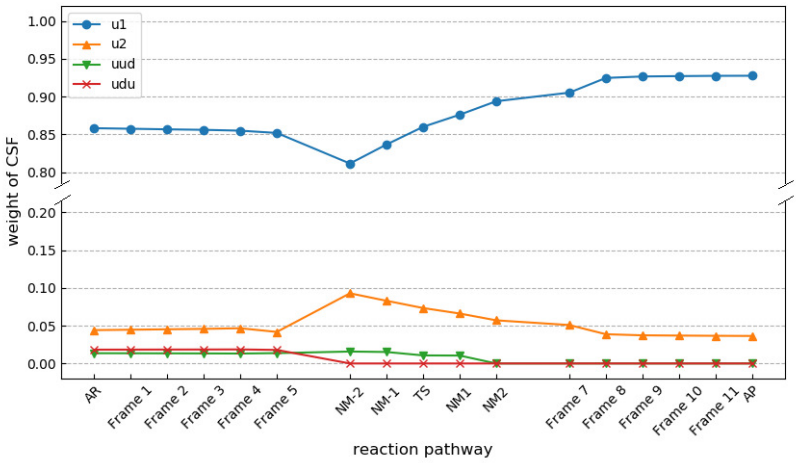


Figure 7: Weights of **u1**, **u2**, **uud**, and **udu** CSFs along the reaction pathway. Weights less than 1 % are omitted.

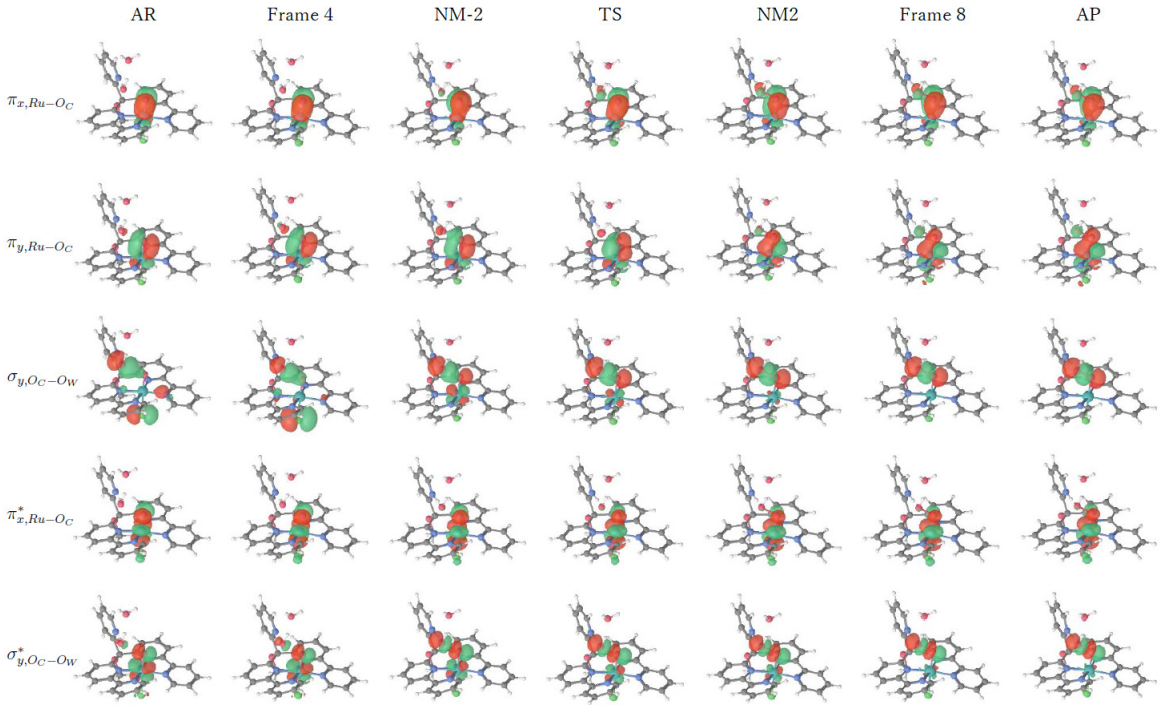


Figure 8: Variations of $\pi_{x,Ru-O_C}$, $\pi_{y,Ru-O_C}$, $\sigma_{y,O_C-O_W}$, $\pi^*_{x,Ru-O_C}$, and $\sigma^*_{y,O_C-O_W}$ NOs along the reaction pathway.

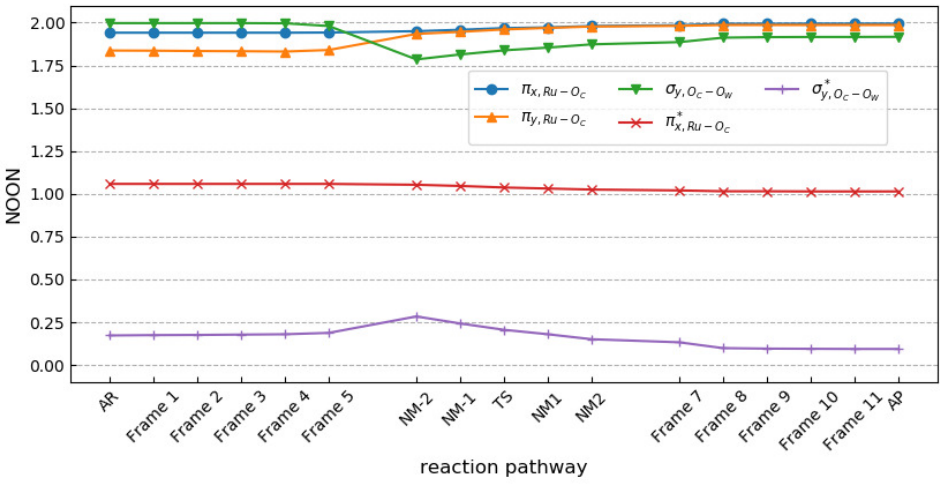


Figure 9: NOONs of $\pi_{x,Ru-O_C}$, $\pi_{y,Ru-O_C}$, $\sigma_{y,O_C-O_W}$, $\pi^*_{x,Ru-O_C}$, and $\sigma^*_{y,O_C-O_W}$ along the reaction pathway.

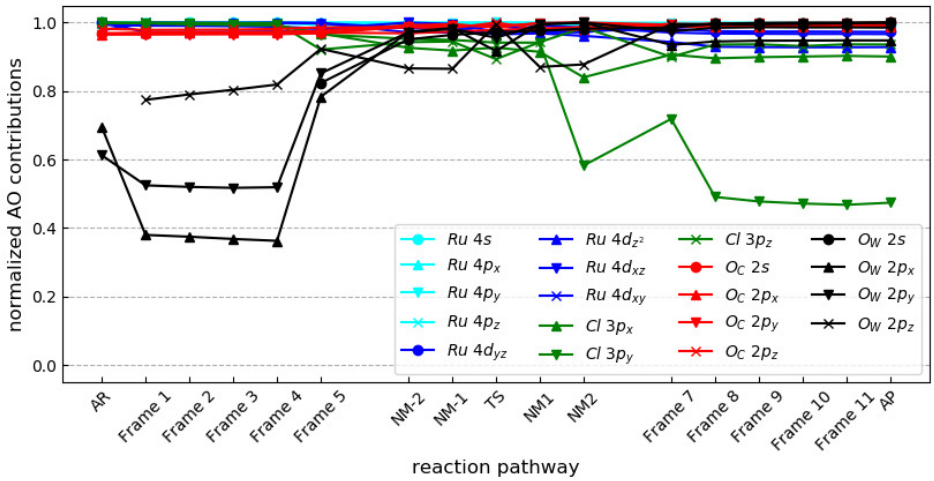


Figure 10: Variation of normalized AO contributions along the reaction pathway. For each AO, normalization is conducted by the division of the highest contribution along the pathway. Contributions less than 0.3 are omitted.

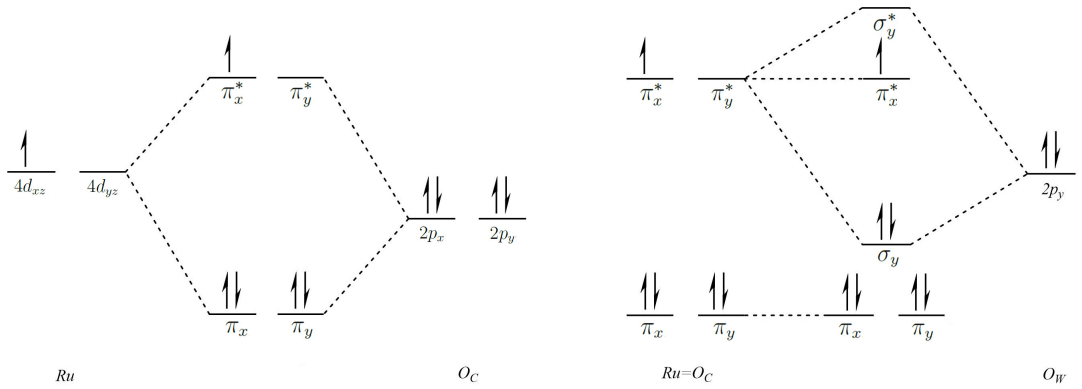


Figure 11: Proposed orbital interaction diagrams for valence orbitals formed by *Ru* and $O_C$ (left) and *Ru*=$O_C$ and $O_W$ (right) with occupations related to the **u1** CSF.

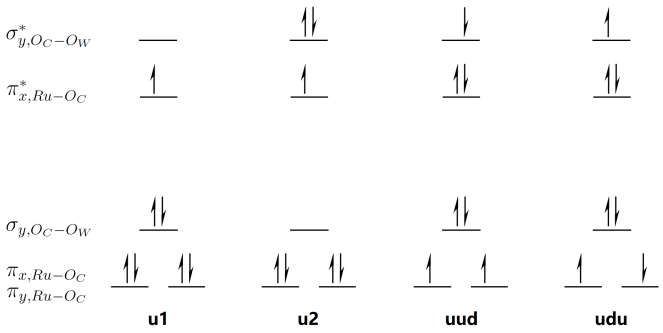


Figure 12: Orbital diagrams of **u1**, **u2**, **uud**, and **udu** CSFs.

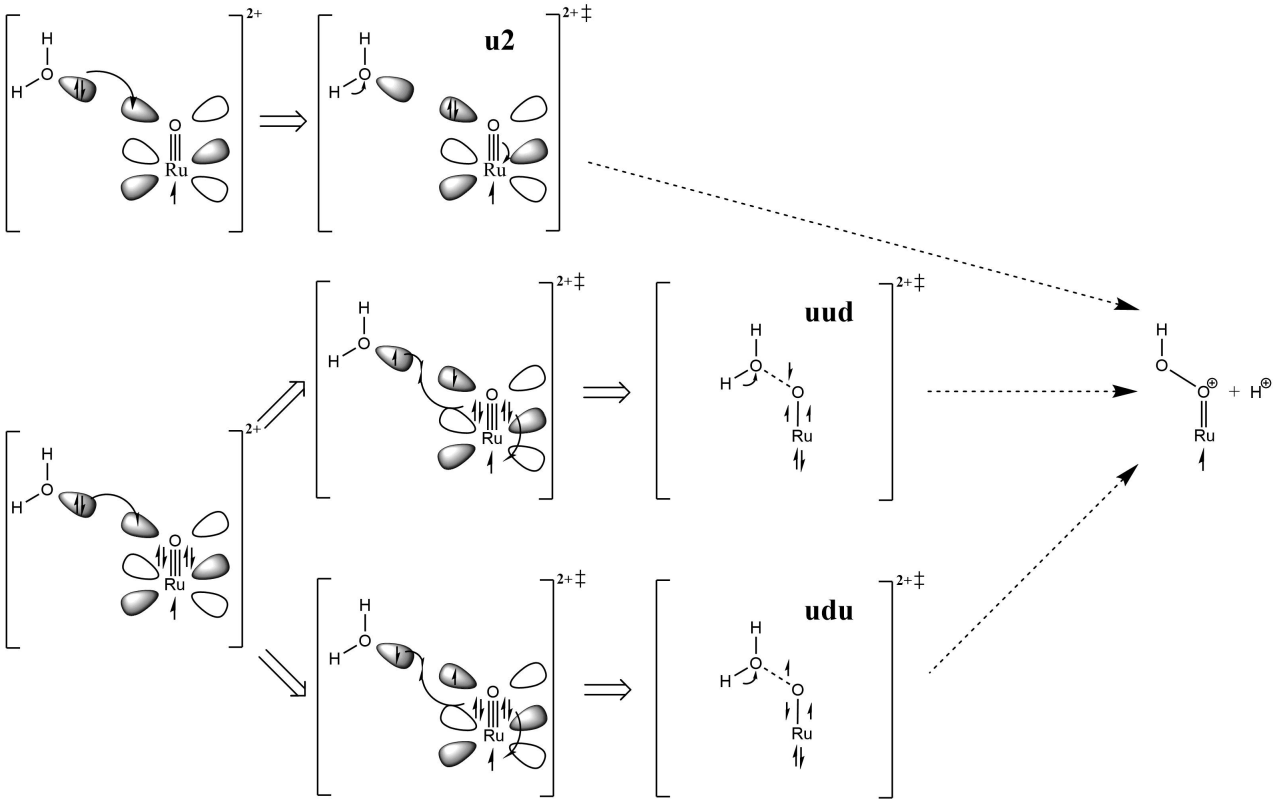


Figure 13: Possible mechanisms of the electron pair process (top) and the single electron processes (bottom).

Table 1: Determination of the active space for the TS structure. The active space did not change during the calculation with CAS(33,19) shown in the last column.

| CAS(27,16) | $\longrightarrow$ | CAS(29,17) | $\longrightarrow$ | CAS(33,19) |
|---|---|---|---|---|
| $Ru\ 4d_{z^2}$ | | $Ru\ 4d_{z^2}$ | | $Ru\ 4d_{z^2}$ |
| $Ru\ 4d_{xy}$ | | $Ru\ 4d_{xy}$ | | $Ru\ 4d_{xy}$ |
| $Ru\ 4d_{xz}$ | | $Ru\ 4d_{xz}$ | | $Ru\ 4d_{xz}$ |
| $Ru\ 4d_{yz}$ | | $Ru\ 4d_{yz}$ | | $Ru\ 4d_{yz}$ |
| | switches in | $Ru\ 4s$ | | $Ru\ 4s$ |
| | switches in | $Ru\ 4p_x$ | | $Ru\ 4p_x$ |
| | switches in | $Ru\ 4p_y$ | | $Ru\ 4p_y$ |
| | switches in | $Ru\ 4p_z$ | | $Ru\ 4p_z$ |
| $Cl\ 3s$ | switches out | | | |
| $Cl\ 3p_x$ | switches out | | switches in | $Cl\ 3p_x$ |
| $Cl\ 3p_y$ | switches out | | switches in | $Cl\ 3p_y$ |
| $Cl\ 3p_z$ | | $Cl\ 3p_z$ | | $Cl\ 3p_z$ |
| $O_C\ 2s$ | | $O_C\ 2s$ | | $O_C\ 2s$ |
| $O_C\ 2p_x$ | | $O_C\ 2p_x$ | | $O_C\ 2p_x$ |
| $O_C\ 2p_y$ | | $O_C\ 2p_y$ | | $O_C\ 2p_y$ |
| $O_C\ 2p_z$ | | $O_C\ 2p_z$ | | $O_C\ 2p_z$ |
| $O_W\ 2s$ | | $O_W\ 2s$ | | $O_W\ 2s$ |
| $O_W\ 2p_x$ | | $O_W\ 2p_x$ | | $O_W\ 2p_x$ |
| $O_W\ 2p_y$ | | $O_W\ 2p_y$ | | $O_W\ 2p_y$ |
| $O_W\ 2p_z$ | | $O_W\ 2p_z$ | | $O_W\ 2p_z$ |

Table 2: Electronic energies of the two schemes along the reaction pathway. Values are relative to the electronic energy of the TS structure. Unit: kcal/mol

| *Geometry* | $Energy_{TSinitial}$ | $Energy_{Framewise}$ |
|---|---|---|
| AR | -17.48 | -17.52 |
| Frame 1 | -16.04 | -16.08 |
| Frame 2 | -14.26 | -14.29 |
| Frame 3 | -12.10 | -12.10 |
| Frame 4 | -8.29 | -8.29 |
| Frame 5 | 4.32 | 4.32 |
| NM-2 | 5.63 | 5.61 |
| NM-1 | 2.72 | 2.72 |
| TS | 0.00 | 0.00 |
| NM1 | -1.98 | -1.98 |
| NM2 | -4.33 | -4.34 |
| Frame 7 | -7.44 | -7.46 |
| Frame 8 | -9.80 | -9.80 |
| Frame 9 | -10.30 | -10.30 |
| Frame 10 | -10.56 | -10.56 |
| Frame 11 | -10.72 | -10.75 |
| AP | -10.84 | -10.84 |

Table 3: NOs concerned in the description of CSFs

| CSFs | Description of the active space | | | | | | | | | |
|---|---|---|---|---|---|---|---|---|---|---|
| **u1** | 2 2 2 2 2 2 2 | 2 | 2 | 2 | 2 2 | 2 | 2 2 2 | u | 0 | 0 |
| **u2** | 2 2 2 2 2 2 2 | 2 | 2 | 2 | 2 2 | 0 | 2 2 2 | u | 2 | 0 |
| **uud** | 2 2 2 2 2 2 2 | u | 2 | u | 2 2 | 2 | 2 2 2 | 2 | d | 0 |
| **udu** | 2 2 2 2 2 2 2 | u | 2 | d | 2 2 | 2 | 2 2 2 | 2 | u | 0 |
| | | ↓ | | ↓ | | ↓ | | ↓ | ↓ | |
| | | $\pi_{x,Ru-O_C}$ | | $\pi_{y,Ru-O_C}$ | | $\sigma_{y,O_C-O_W}$ | | $\pi^*_{x,Ru-O_C}$ | $\sigma^*_{y,O_C-O_W}$ | |

Table 4: Estimated bond orders of $Ru$=$O_C$ and $O_C$-$O_W$ in the four major CSFs. Bond orders are calculated by $\boldsymbol{B.O.} = \frac{1}{2}(\boldsymbol{N}_{bonding\ electrons} - \boldsymbol{N}_{antibonding\ electrons})$ with NOs sketched in Fig. 8 and Fig. 12. Except of the $\pi$-type bonds mentioned in the orbital diagram in Fig. 12, a $\sigma$-type bond between $Ru$ and $O_C$ is also counted in the bond order.

| Bond | **u1** | **u2** | **uud** | **udu** |
|---|---|---|---|---|
| $Ru$=$O_C$ | +2.5 | +2.5 | +1.0 | +1.0 |
| $O_C$-$O_W$ | +1.0 | -1.0 | +0.5 | +0.5 |